Draft version December 7, 2023
Typeset using LATEX **twocolumn** style in AASTeX631

Evolution of Flare Rates in GKM Stars Younger than 300 Myr

Adina D. Feinstein[1,*]

[1]*Laboratory for Atmospheric and Space Physics, University of Colorado Boulder, UCB 600, Boulder, CO 80309*

ABSTRACT

Stellar flares are short-duration ($<$ hours) bursts of radiation associated with magnetic reconnection events. The magnetic activity of stars is known to decrease as a function of age and Rossby number, R_0, a parameterization of how strong the Coriolis force is. Here, we detect and characterize the flare properties of $\sim$ n stars younger than 300 Myr which have been observed by the Transiting Exoplanet Survey Satellite at 2-minute cadence. Our stars are bona fide, high-probability, or candidate members of 26 nearby young moving groups, clusters, or associations. We identified n flares originating from n stars. We robustly measured the rotation periods of $1,847$ stars. We measure the flare frequency distribution (FFD) slope as a function of both age and spectral type. We find the FFD slope, α, saturates for all spectral types at $\alpha = -0.5$ and does not evolve over 300 Myr. Additionally, we find that R_0 and flare rate for stars $t_{\text{age}} = 100 - -300$ Myr are saturated out to $R_0 = 0.12$, which is consistent with other indicators of magnetic activity. We find the FFD slope for stars with $R_0 \leq 0.12$ are shallower than stars with $R_0 > 0.12$, suggesting the Coriolis force plays a role in generating more high-energy flares. We cross match our targets with *GALEX* and find no correlation between flare rate and Far- and Near-Ultraviolet flux. Finally, we compare the flare rates of planet hosting stars to comparable, larger samples of stars and find the majority of these stars are relatively flare quiet. This may impact the atmospheric evolution of young short-period exoplanets.

1. INTRODUCTION

Stellar flares are the radiation component of magnetic reconnection events (). Such events are readily seen on the Sun (), particularly now as we enter a maximum in the solar cycle (). Such events can be used to understand the magnetic activity of other stars (). Additionally, by studying stellar flares we can understand how these short-duration events may impact short-period exoplanet evolution (). While we cannot resolve stellar flare events on other stars, we can detect and characterize both spectroscopic and photometric signatures of such events. Spectroscopic characterization of stellar flares inform our understanding of non-thermal processes affiliated with such events, e.g. coronal mass ejections () or proton beams (). They can also inform our understanding of stellar plasma is displaced during these events ().

Photometric observations of stars are more readily available thanks to exoplanet missions, and allow us to statistically characterize flare rates and energies. Within time-series photometry, stellar flares can be identified by a sharp rise in the stellar flux and a subsequent exponential decay, corresponding to the cooling rate (). *Kepler* provided long-baseline high-cadence observations used to identify stellar flares. There has been extensive studies of flares in *Kepler* data, from the statistics of superflares on solar-type stars (Notsu et al. 2013; Shibayama et al. 2013; Maehara et al. 2015; Okamoto et al. 2021, e.g.) to low-mass stars (Hawley et al. 2014; Silverberg et al. 2016, e.g.). Davenport et al. (2019) found that flare activity decreased with increasing rotation period for 347 GKM stars. However, the flare frequency distribution (FFD) slope did not change significantly as a function of age. As a caveat, the ages of the stars were determined based on their rotation periods alone, relying on the assumption that gyrochronology alone accurately ages stars.

After the failure of two reaction wheels, *Kepler* was repurposed to the *K2* mission (Howell et al. 2014). *K2* provided 70-day baseline observations for a handful of young stars in groups such as Upper Scorpius, Pleiades, Hyades, and Praespe clusters. Ilin et al. (2019) analyzed flares K and M stars in these clusters and measured FFD slopes of ...

More recently, the Transiting Exoplanet Survey Satellite (TESS; Ricker et al. 2015) has provided near all-sky photometric observations at 30-minute cadence or less. Such an observing strategy has allowed for more detailed

[*] NHFP Sagan Fellow

studies of young stellar flares from nearby young moving groups and associations, which are disperse in the sky ().

The paper is presented as follows. In Section 2, we describe our sample, stellar flare identification and fitting methods, and methods for measuring stellar rotation periods. In Section 3, we present our flare-frequency distribution (FFD) fits as a function of stellar age, $T_{\rm eff}$, and R_0. In Section 4, we search for correlations in flare rates with FUV and NUV observations from *GALEX* and place the flare rates of young planet hosting stars in the context of our broader sample. We conclude in Section 5. We provide additional figures and tables in Section A.

2. METHODOLOGY

2.1. *Sample Selection*

We aim to measure the evolution in flare rates as a function of stellar age for stars with $1 \leq t_{\rm age} \leq 250$ Myr. We used the MOCA Data Base (Gagné et al. in prep.) to identify nearby young moving groups, associations, and open clusters with known ages which satisfied our criteria. We identified unique 26 groups from which we created our sample list. We considered all targets that are either bona fide members, high-likelihood candidate members, or candidate members. This resulted in a catalog of 30,889 stars across 26 associations. We summarize the sample and quote adopted ages for each association in Table 1.

Table 1. Adopted Ages of each Young Stellar Population and Number of Stars per Group

Population	Age [Myr]	$N_{\rm stars}$	Ref.
AB Doradus	133^{+15}_{-20}	81	1
Blanco 1	$137.1^{+7.0}_{-33}$	301	8
Carina	45	91	2
Carina-Musca	32	22	5
Chamaeleon	5	366	3
Columba	42	126	2
Greater Taurus Subgroup 5	8.5	56	5
Greater Taurus Subgroup 8	4.5	114	5
Lower Centaurus Crux	15	590	4
MELANGE-1	250^{+50}_{-70}	22	10
Octans	35±5	98	6
Pisces Eridanis	120	176	7
Pleiades	$127.4^{+6.3}_{-10}$	1304	8
α Persei	$79^{+1.5}_{-2.3}$	467	8
IC 2602 corona	$52.5^{+2.2}_{-3.7}$	10	8
IC 2602 system	$52.5^{+2.2}_{-3.7}$	138	8
NGC 2451A	48.5	44	5
Oh 59	162.2	50	9
Platais 9	50	99	11
RSG2	126	87	12
Theia 301	195	372	9
Theia 95	30.2	191	9
TW Hydrae	10	24	2
Upper Centaurus Lupus	16	464	4
Upper Scorpius	10	80	4
Vela-CG4	33.7	352	5

NOTE—Age references: (1) Gagné et al. (2018); (2) Bell et al. (2015); (3) Luhman (2007); (4) Pecaut & Mamajek (2016); (5) Kerr et al. (2021); (6) Murphy & Lawson (2015); (7) Curtis et al. (2019); (8) Galindo-Guil et al. (2022); (9) Kounkel et al. (2020); (10) Tofflemire et al. (2021); (11) Tarricq et al. (2021); (12) Röser et al. (2016);

2.2. *TESS Light Curves*

To ensure we were able to resolve and accurately measure the energies of flares on these stars (Howard & MacGregor 2022), we used the 2-minute data from the TESS mission. We crossmatched our sample with the TESS Input Catalog (TIC) based on their RA and Dec. We considered a star to be in the catalog if the distance between the target and the nearest TIC was within 1". This resulted in a final sample of 5,725 unique targets which have been observed at 2-minute cadence between Sector 1 and Sector 67, the latest available sector upon this analysis. Given the proximity of many targets towards the northern and southern ecliptic poles (Figure 1), many targets were observed over multiple sectors. We downloaded all available data, yielding a total of 17,964 light curves.

2.3. *Flare Identification*

We followed the machine learning flare-identification methods presented in **?**. This method relies on the fact that all flare events have similar time-dependent morphologies generally described as a sharp rise and an exponential decay. This method uses a convolutional neural network (CNN), `stella` (Feinstein et al. 2020), trained on by-eye validated flare events from TESS Sectors 1 and 2 to identify flare events in TESS 2-minute data (Günther et al. 2020; **?**). The benefits of the CNN is that it is insensitive to the stellar baseline, since it is trained to look only for the flare morphology. This means that the peaks of rotational modulation driven by stellar heterogeneities, which is readily seen in the light curves of young stars, are not accidentally identified as flares. In this way, we are able to build a sample of flares which is unbiased towards low-amplitude/low-energy flares, which are often not identified in traditional sigma-outlier identification methods (Chang et al. 2015).

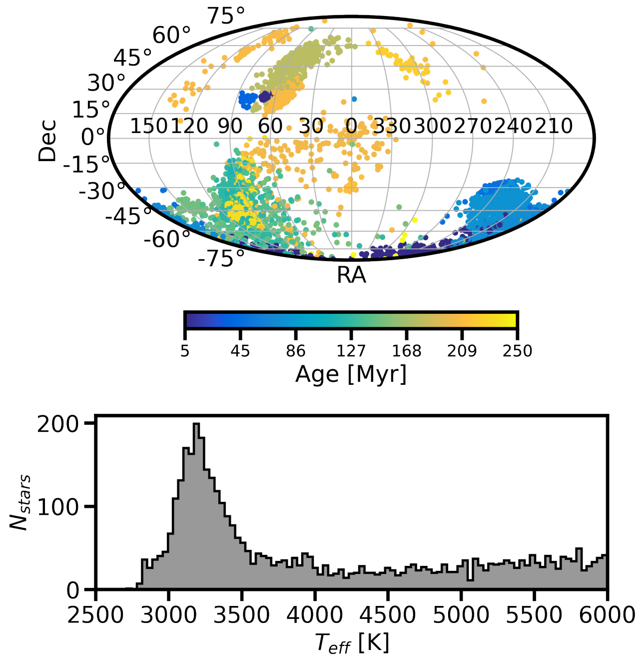

Figure 1. Distribution of our selected sample across the sky and colored by the adopted age of the association (see Table 1). The all-sky coverage by TESS has unlocked new populations of stars to observe. We take advantage of this observing strategy to measure flare rates across 26 different nearby young moving groups, clusters, and associations.

The `stella` CNN models take the light curve (time, flux, flux error) as an input and returns an array with values of [0,1], which are treated as the probability a data point is (1) or is not (0) part of a flare. We ran all light curves through 10 `stella` models and averaged the output, taking this as the final prediction per observation. The `stella` code uses the predictions per data point to group together points, identifying those as single flare events. It then calculates the probability of the entire flare event as the average of the probabilities assigned to all the data points during the flare.

2.3.1. *Modeling Flare Properties*

We used the analytical flare model in Tovar Mendoza et al. (2022)[1] to fit the flares in our sample. This model builds upon the model presented in Davenport et al. (2014), and includes a convolution of a Gaussian with a double exponential model. The analytical model accounts for the amplitude, heating timescale, rapid cooling phase timescale, and slow cooling phase timescale of flares. Using this model, we used a non-linear least squares optimization to fit for the time of the flare peak ($t_{\rm peak}$), full width at half maximum (FWHM), and the amplitude (A), of each flare in the sample. We combine

[1] https://github.com/lupitatovar/Llamaradas-Estelares

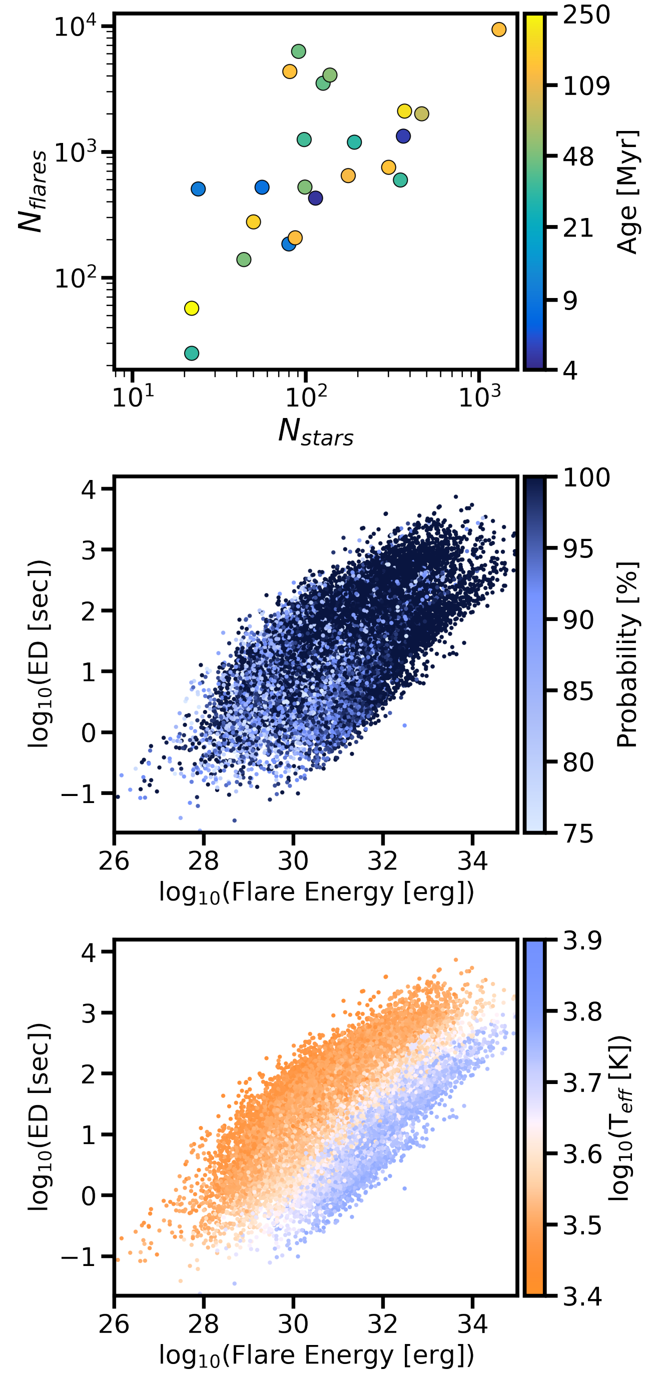

Figure 2. High level summary of the demographics of flares in our sample. Top: The number of flares identified compared to the number of stars in each nearby young moving group, cluster, or association. A one-to-one relationship is expected. Middle: The distribution measured TESS energies and equivalent durations of flares in our sample, colored by the probability of the flare as identified with `stella`. Bottom: Same as the middle plot, except colored by the $T_{\rm eff}$ [K] of the star. We limit our sample to stars with $T_{\rm eff} \leq 6000$ K.

the model with a second-order polynomial fit to a 10-hour baseline before and after the flare to account for any rotational modulation.

2.3.2. *Flare Quality Checks*

The `stella` CNNs were initially trained on data from TESS Sectors 1 and 2. Because the noise properties from sector to sector varies, the CNNs are unable to accurately capture all of these changes. Additionally, the CNNs were trained on a sample of n stars, which does not necessarily encapsulate all types of variable stars or a sufficient distribution of variable stars (e.g., eclipsing binaries and RR Lyraes). As such, we apply the additional quality checks presented in Feinstein et al. (2022) to ensure our flare sample has little to no contamination from other sources. We remove flares which satisfy the one or more of the following criteria:

1. The amplitude of the flare must be > 0.01, or 1%. This follows the limits set by Feinstein et al. (2020).

2. The amplitude of the flare (A) must be greater than 1.5×CDPP (Combined Differential Photometric Precision; Christiansen et al. 2012), similar to Feinstein et al. (2022).

3. For flares originating from stars with $T_{\rm eff} > 5000$, the amplitude of the flare must be greater than 12×CDPP. This is because the most massive stars tended to have much larger scatter in the TESS noise.

4. The fitted equivalent duration (ED) must be positive ED > 0.

5. The fitted full-width half-maximum (FHWM) and A must be > 0.

6. The error on the A must be $\sigma_A < A$. This removed poorly constrained flares and often flares which were buried in the TESS noise.

We choose to include flares with a probability $P \geq 75\%$ of being a true flare. After these checks, we have a flare sample of 28,822 flares originating from 3,979 stars (Figure 2). 83.8% of the flares have probabilities of $P \geq 90\%$ of being true; 65.0% of the flares have probabilities of $P \geq 99\%$ of being true.

2.4. *Measuring Rotation Periods*

Seligman et al. (2022) demonstrated that stars with low Rossby numbers $R_0 < 0.13$ have shallower flare frequency distribution slopes, indicative of more high energy flares originating from these sources. In addition to understanding flare statistics across young ages, we aim to expand this sample by measuring the rotation periods, $P_{\rm rot}$, for the stars in our sample. To do this, we used `michael`[2], an open-source Python package that robustly measures $P_{\rm rot}$ using a combination traditional Lomb-Scargle periodograms and wavelet transformations (Hall et al. submitted). `michael` measures $P_{\rm rot}$ using the `eleanor` package, which extracts light curves from the TESS Full-Frame Images (FFIs; Feinstein et al. 2019). We ran `michael` on all stars from which flares were identified. The estimated $P_{\rm rot}$ were vetted by-eye, from the `michael` diagnostic plots. In total, we robustly measured 1,269 $P_{\rm rot}$ across our sample of 3,983 stars, which is $\sim 50\%$.

3. RESULTS

We analyze our new flare sample from three perspectives. First, we perform the standard FFD fitting of a power-law to the distribution of flare energies. Second, we fit the FFD with the prescription in Gershberg (1972), which fits for both the FFD slope and y-intercept. Third, we fit a truncated power-las to the distribution of flare amplitudes, to determine if there is a correlation between R_0 and flare distributions.

The number of stars, and consequently flares, per each association varied greatly, due to the limited number of stars observed at TESS 2-minute cadence. Therefore, instead of measuring FFD properties as a function of association, we opted to group stars by effective temperature, $T_{\rm eff}$, and average adopted association age. We grouped stars in the following $T_{\rm eff}$ space: M-stars below the fully convective boundary ($T_{\rm eff} = 2300 - 3400$ K), early type M-stars ($T_{\rm eff} = 3400 - 3850$ K), late K-stars ($T_{\rm eff} = 3850 - 4440$ K), early K-stars ($T_{\rm eff} = 4440 - 5270$ K), and G-stars ($T_{\rm eff} = 5270 - 5930$ K). We did not include any stars hotter than $T_{\rm eff} > 5930$ K, as these stars are dominated by noise in the TESS observations. Additionally, we grouped stars in the following age space: $4 - 10$ Myr, $10 - 20$ Myr, $20 - 40$ Myr, $40 - 50$ Myr, $70 - 80$ Myr, $120 - 150$ Myr, and $150 - 300$ Myr. We note that there is a gap in age from $50 - 70$ Myr, which could be expanded with the identification of more associations in this age range. However, for the purposes of this work, we do not include additional sources which may fall in this age range.

3.1. *Standard Power-Law Fits*

From the $T_{\rm eff}$ and age bins described above, we binned the flares in each subgroup and fit their FFD slopes,

[2] https://github.com/ojhall94/michael

approximated as a power-law. Flares were binned into 25 bins in log-space from $10^{27} - 10^{35}$ erg. We fit the FFDs from the energy bin with the maximum flare rate and energies higher than that. We opt to do this as bins of lower energies may be incomplete, and the turnover in the FFD cannot be accurately modeled as a power-law.

We fit the FFD using the MCMC method implemented in `emcee` (Goodman & Weare 2010; Foreman-Mackey et al. 2013) and fit for the slope, α, y-intercept, b, and an additional noise term, f, which accounts for an underestimation of the errors on each bin. We initialized the MCMC fit with 300 walkers and ran our fit over 5000 steps. Upon visual inspection, we discarded the first 100 steps; onwards the steps were fully burned-in. The full FFDs are presented in Figure A1, along with 100 samples from the MCMC fit. The measured FFD slopes, α are presented in Figure 3. We approximate the error on the slope as the lower 16^{th} and upper 84^{th} percentiles from the MCMC fit.

There is a 3σ discrepancy between the FFD slope measured in Ilin et al. (2021) and the work presented here at ages ~ 120 Myr. This discrepancy could be the result of several factors. First, Ilin et al. (2021) used the *K2* 30-minute light curves. This would result in a sample biased towards the highest-energy flares which could be sampled at this cadence. Our flare detection method is less-biased towards the low-energy flares due to the 2-minute cadence from TESS and our flare detection algorithm. Second, our sample has $\sim 2\times$ the number of stars and $\sim 7\times$ the number of flares than their sample. This could result in a more complete FFD compared to previous work.

3.2. *Truncated Power-Law Fits*

We follow the prescription presented in Seligman et al. (2022). Namely, we fit a truncated power-law distribution of the form

$$dp/dA \propto A^{-\alpha_T} e^{-A/A_*} \tag{1}$$

where A is the amplitude of the flare, A_* is a flare amplitude cutoff parameter and α_T is the slope, rather than α. We fit the slopes using the MCMC method implemented in `emcee` (Goodman & Weare 2010; Foreman-Mackey et al. 2013), using the log-likelihood function in Seligman et al. (2022). We fit for A_* and α_T. We initialized the MCMC fit with textcolorredn walkers and evaluated the fit over textcolorredn steps. The first textcolorredn steps were discarded upon visual inspection. The results are presented in Figure 4.

3.3. *Flare Rates Compared to R_0*

The Rossby number, R_0, is a term which marginalizes over several properties which are known to affect the stellar dynamo, such as the rotation period and stellar mass. We convert our measured rotation periods to R_0, which is defined as $R_0 = P_{\text{rot}}/\tau$, where τ is the convective turnover time. We approximate τ following the prescription in Wright et al. (2011). We equate the flare rates for individual stars as

$$\mathscr{R} = \frac{1}{t_{\text{obs}}} \left(\sum_{i=1}^{N} p_i \right) \tag{2}$$

where $\mathscr{R}$ is the flare rate in units of day^{-1}, t_{obs} is the total amount of time a target was observed with TESS, and p_i is the probability that flare i is a true flare as assigned by `stella`. We compare the calculated R_0 to measured flare rates for all stars we measured P_{rot} for. The results are presented in Figure 5.

We evaluate the relationship between age, spectral type, flare rate, and R_0. We divide the sample between stars younger and older than 50 Myr, which roughly correlates to the age at which GKM stars turn onto the main sequence. For stars younger than 50 Myr, we find the flare rate slightly decreases with increasing R_0, although there is a significant amount of scatter in this relationship. For stars between $50 - 250$ Myr, we see this relationship much clearer. For M stars, we see minimal evolution in both average flare rate and R_0 between the two samples. For K stars, we see R_0 evolving over the first 250 Myr, while the scatter in the flare rate decreases. For G stars, we see the scatter in R_0 decreasing, and the average flare rate across the sample decreases. We present a compiled histogram for all stars in our sample in the right column of Figure 5.

To better understand this trend, we fit three types of functions: (i) a constant value, (ii) a single power law, and (iii) a piece-wise function consisting of a constant value and a power law. For (iii), we computed these fits across a range of R_0 for where the turnover should occur. We binned the cumulative dataset consisting of all GKM stars into 50 evenly-spaced bins in log-space from $log_{10}(R_0) = [-2, 0]$. We computed the χ^2 between each of these fits and the data. For stars $4.5 - 50$ Myr, we find the distribution is best-fit with a single power law with slope $m = -0.243 \pm 0.043$ and y-intercept $b = -1.221 \pm 0.061$. Converting the χ^2 to a standard deviation, we find a single fit is preferred by $\sim 3\sigma$. For stars $50 - 250$ Myr, we find the distribution is best-fit with a piece-wise function of the form

$$\mathscr{R} = \begin{cases} C & R_0 \leq 0.15 \\ 10^b * R_0^m & R_0 > 0.15 \end{cases} \tag{3}$$

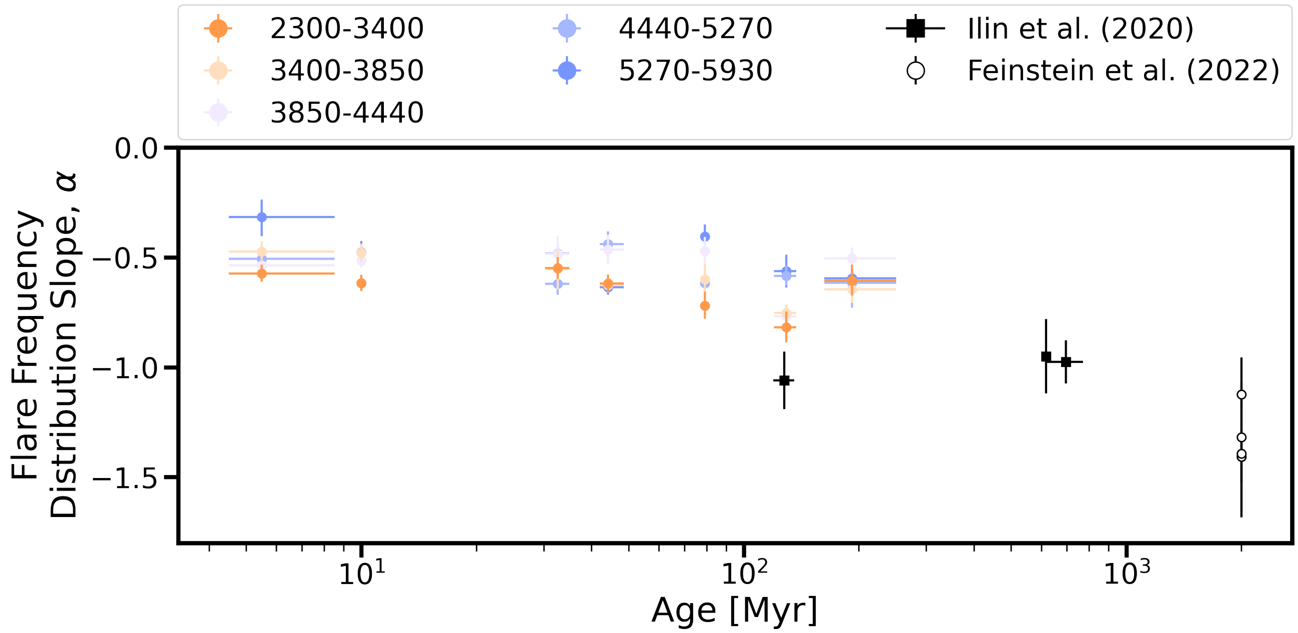

Figure 3. Measured flare-frequency distribution slopes, α, as a function of stellar effective temperature, $T_{\rm eff}$ and age.

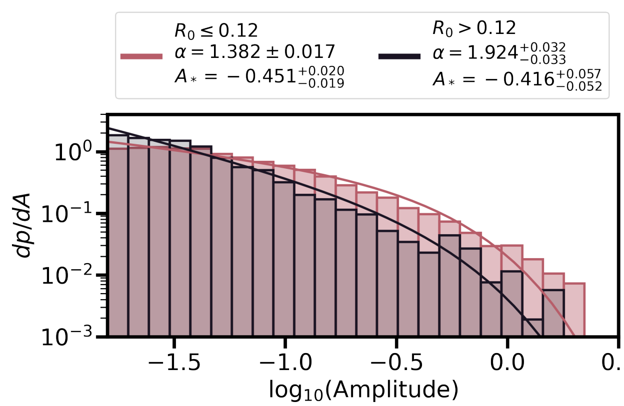

Figure 4. Flare frequency distributions, as a function of flare amplitude, for stars with $R_0 \leq 0.12$ (red) and stars with $R_0 > 0.12$ (black). We present the best-fit model, and the best-fit values of the model slope and normalization factor in the legends. Our sample of $R_0 \leq 0.12$ includes 13,132 flares from 800 stars; our sample of $R_0 > 0.12$ includes 5,603 flares from 747 stars. We find the stars with smaller Rossby numbers have shallower slopes, consistent with more, high-energy flares and potentially larger convective regions (Seligman et al. 2022).

where $\mathscr{R}$ is the flare rate, $C = 0.126 \pm 0.006$, $m = -0.986 \pm 0.119$, and $b = -1.687 \pm 0.078$. We test how our bin size affected our R_0 turnover. To do this, we refit our data assuming binning from $20 - 100$ bins and find R_0 to be consistent with $R_0 = 0.15 \pm 0.02$. The location of the turnover is consistent to within 1σ with what has been seen in other observations of magnetic saturation for partially and fully convective stars (e.g. $L_X/L_{\rm bol}$; Wright et al. 2018).

4. DISCUSSION

4.1. *Correlations with Far- and Near-Ultraviolet Flux*

X-ray luminosity surveys of stars have revealed a saturation limit with respect to the star's rotation period. Namely, there is no evolution in $L_X/L_{\rm bol}$ for stars with $P_{\rm rot} < 10$ days (Pizzolato et al. 2003).

The Far- and Near-Ultraviolet (FUV/NUV) is another tracer of magnetic activity. Young stars are known to have excess luminosity in both of these wavelengths (). We use archival observations from the *Galaxy Evolution Explorer* (*GALEX*; Martin et al. 2005) to search for trends in FUV/NUV saturation and flare rate saturation. *GALEX* provides broad FUV photometry from $1350 - 1750$Å and NUV photometry from $1750 - 2750$Å. We crossmatch our targets with the *GALEX* catalog. We follow the sample selection methods outline in (Schneider & Shkolnik 2018). We search a $10''$ radius around the coordinates of each target in our sample. We include targets with no bad photometric flags (e.g. `fuv_artifact` or `nuv_artifact == 0`) as defined in the catalog. This is recommended by the *GALEX* documentation, as flags could be assigned due to bright star window reflection, dichroic reflection, detector run proximity, or bright star ghost. We exclude targets with measured magnitudes brighter than 15, which marks the saturation limit for both the FUV and NUV photometers (Morrissey et al. 2007).

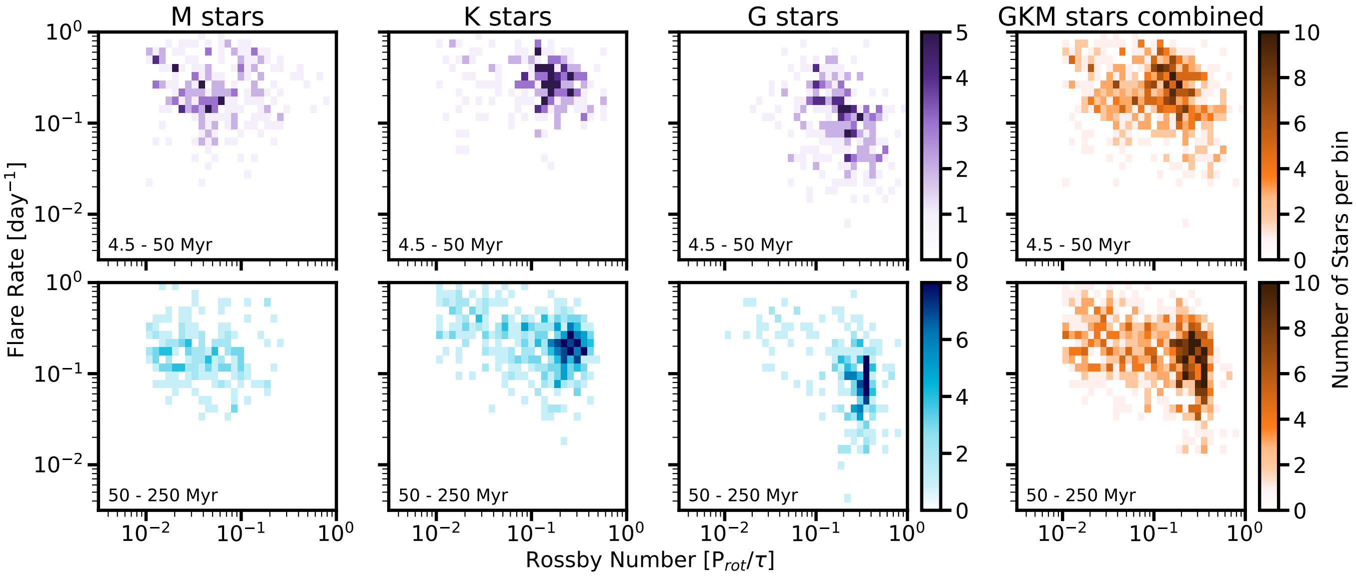

Figure 5. Comparison of Rossby Number, R_0 and flare rate for young GKM stars. We find no change in the average flare rate for GKM stars < 250 Myr. We see evidence that as R_0 increases, the average flare rate decreases. This is similar to results presented in Medina et al. (2020), however our sample extends this trend to young GKM stars, while previous results were limited to nearby M dwarfs. The top row are stars with ages $4.5 - 50$ Myr; the bottom row are stars with ages $50 - 250$ Myr. The histograms are colored by number of stars in each bin.

Based on these thresholds, we find that 462 stars in our sample have NUV photometry and 139 stars have FUV photometry. We explore if flare rate saturation and FUV/NUV saturation are correlated with the derived R_0 per star. We present our results in Figure 6. We present the measured FUV/NUV flux normalized by the J-band flux of the star, since it is the fractional flux which acts as an activity indicator. While bolometric luminosities would be a better normalizing factor, we find the majority of stars in our target do not have this parameter measured. To assess FUV/NUV correlations in a larger statistical sense, we thus keep the normalization to f_J.

4.2. *Comparison to Young Planet Host Stars*

The all-sky observing strategy of TESS has revealed a new population of young transiting exoplanets. Characterizing the local environment for these planets is crucial to understanding their subsequent evolution to forming the mature population of planets. It is debated whether stellar flares are beneficial or detrimental to exoplanets. On one hand, creates life. On the other hand, stellar flares and affiliated coronal mass ejections can permanently alter atmospheric compositions (Chen et al. 2021) and increase the amount of atmospheric mass stripped during the early stages of planet evolution (Feinstein et al. 2020). To understand the evolution of these new insightful young transiting exoplanets, we compare their measured flare rates to a more statistical sample of stars with similar ages and $T_{\rm eff}$.

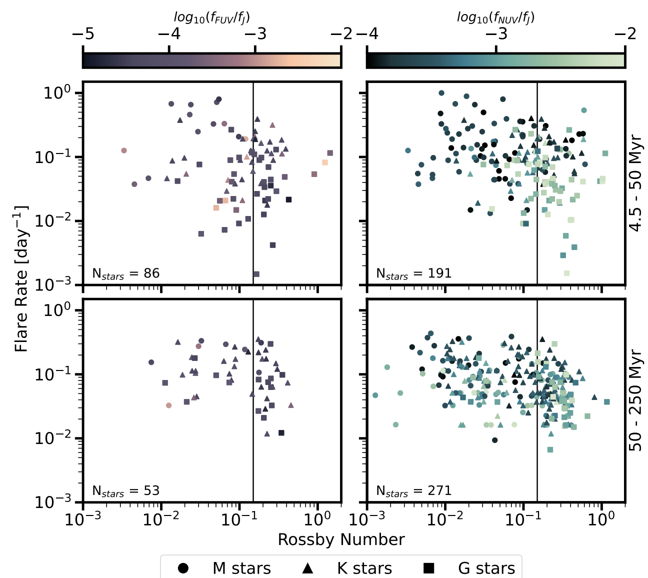

Figure 6. Calculated FUV (left) and NUV (right) GALEX flux for stars in our sample. We normalize these values by the J-band flux of the star. We find no strong correlation between the NUV/FUV flux and the measured flare rate or Rossby number. The top row shows GKM stars $<$ 50 Myr; the bottom row shows GKM stars $\geq$ 50 Myr. M stars are shown as circles, K stars as triangles, and G stars as squares. We note that f_{NUV} traces the photosphere of GK stars, and therefore may not be the best comparison bandpass when looking for trends in magnetic activity.

We measured the flare rates of planet hosting stars < 300 Myr, comparable to the ages of our primary sample. We followed the methods outlined in Section 2 to detect and vet flares. For each star, we created an equivalent sample with respect to both age and T_{eff} to compare the flare rates too. We considered stars with ages ± 30 Myr of the planet hosting star and $T_{\text{eff}} \pm 1000$ K. We calculate the flare rate following Equation 2. We present the flare rates of planet-hosting stars and a comparable sample of stars in Figure 7 and report the measured rates in Table 2. For the comparable sample, we report the median flare rate, and the lower 16^{th} and upper 84^{th} percentiles.

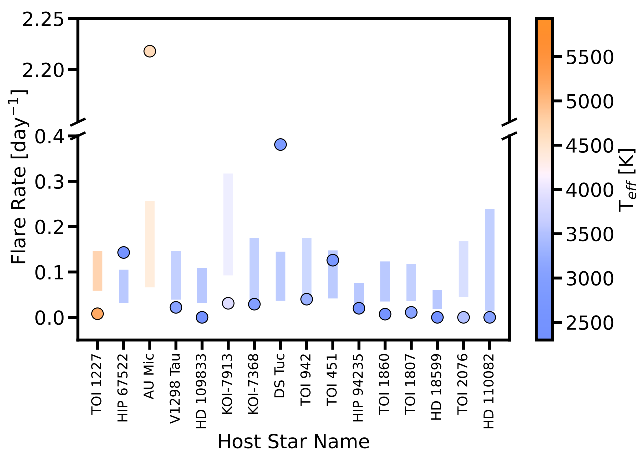

Figure 7. Comparison of flare rates from young planet host stars with respect to a comparable sample with respect to age [Myr] and T_{eff} [K]. Circles represent the flare rate of the host star (name along the x-axis); vertical bars represent the lower 16^{th} and upper 84^{th} percentiles for the comparable sample. The majority of young planet hosting stars have flare rates towards the lower end of the comparable sample's distribution. A handful of hosts have more flares, including HIP 67522, AU Mic, DS Tuc A, and TOI 451. We find no correlation between age or T_{eff} that may result in young planet hosts having more or fewer flares than a larger comparable sample. The measured flare rates are presented in Table 2.

4.3. *Evidence of Stellar Cycles*

The Sun goes through a 12-year solar cycle, which oscillates between times of high and low activity. The solar cycle manifests itself in a variety of observables, including a change in the flare rate, by a factor of 10 (), and the flare energies released (). Constraints of stellar cycles have predominantly relied on photometry (see recent review by **?**). However, tracing stellar cycles via stellar flares may be more reliable, as flares are a direct consequence of magnetic activity. explored measuring the stellar cycle length of KIC 8507979, a star in the *Kepler* field which was observed for 18 90-day quarters. They found the flare rate decreased over each quarter, which could be fit by $L_{\text{fl}}/L_{\text{Kp}} = (-9.96 \pm 3.94) \times 10^{-2} \times t_{\text{yr}} + (2.43 \pm 0.11)$, where t_{yr} is the time in years, and $L_{\text{fl}}/L_{\text{Kp}}$ is a parameterization of the *Kepler* flare rate as defined by (Hawley et al. 2014).

Table 2. Young Planet Host Flare Rates

Host Name	Age [Myr]	Flare Rate [day^{-1}]	Comp. Sample Flare Rate [day^{-1}]
TOI 1227	11 ± 2	0.008	$0.119^{+0.148}_{-0.046}$
HIP 67522	17 ± 2	0.169	$0.046^{+0.069}_{-0.020}$
AU Mic	22 ± 3	2.218	$0.133^{+0.171}_{-0.046}$
V1298 Tau	23 ± 4	0.022	$0.074^{+0.091}_{-0.033}$
HD 109833	27 ± 3	0.000	$0.046^{+0.070}_{-0.020}$
KOI-7913	36 ± 10	0.031	$0.134^{+0.162}_{-0.045}$
KOI-7368	36 ± 10	0.029	$0.064^{+0.087}_{-0.030}$
DS Tuc	45 ± 4	0.420	$0.056^{+0.078}_{-0.024}$
TOI 942	50^{+30}_{-20}	0.040	$0.086^{+0.117}_{-0.038}$
TOI 451	120 ± 10	0.128	$0.071^{+0.085}_{-0.029}$
HIP 94235	133^{+15}_{-20}	0.020	$0.051^{+0.079}_{-0.017}$
TOI 1860	133 ± 26	0.008	$0.067^{+0.086}_{-0.025}$
TOI 1807	18040	0.013	$0.060^{+0.085}_{-0.022}$
HD 18599	200^{+200}_{-70}	0.000	$0.025^{+0.044}_{-0.015}$
TOI 2076	204 ± 50	0.000	$0.092^{+0.091}_{-0.045}$
HD 110082	250^{+50}_{-70}	0.000	$0.047^{+0.067}_{-0.020}$

It is possible that the length of the stellar cycle is related to the $P_{\text{rot}}/\ R_0$ of the star as ... (). If this is the case, then stars with P_{rot} will have shorter stellar cycle lengths. The TESS Extended Mission has provided a five-year baseline, similar to *Kepler*, although the sampling is sparser. Within our sample of fast rotators, we searched for evidence of stellar cycles. Our sample contains 31 stars which have been observed for $t_{\text{obs}} \geq 400$ days and $n_{\text{flare}} > 100$.

We search for evidence of changes in the stellar magnetic activity by looking at (i) the maximum flare energy in a given period of time and (ii) the flare rate over that same period of time. We grouped our observations by year observed, even if the star was not continuously observed throughout that year.

5. CONCLUSIONS

In this work, we present the first measured flare rates for stars < 300 Myr using TESS 2-minute cadence observations. We identified originating 28,822 flares from 3,983 stars. The results of our work are summarized as follows:

1. We measured the flare-frequency distribution (FFD) slope, α, for samples of flares binned by age and T_{eff}. We find α saturates at $\alpha = -0.5$ for stars younger than 300 Myr and declines after that age. This is the first evidence that, like other tracers of stellar magnetic activity, flare rates saturate across spectral types.

2. We measured the y-intercept, β, for the same bins of flares. We find that ...

3. We measured the rotation periods, P_{rot} for n stars in our sample using the open-source Python package `michael`.

4. We measured the slope of a truncated power-law, α_T, for the same bins of flares. Additionally, we measured α_T as a function of Rossby number, R_0.

We thank Darryl Seligman and David Wilson for thoughtful insights and useful conversations. This work made use of the open-source package, *showyourwork!* (Luger et al. 2021), which promotes reproducible publications. ADF acknowledges funding from ...

APPENDIX

A. SUPPLEMENTAL MATERIAL

Miscellaneous figures and such that people might want but I don't need to show

REFERENCES

Bell, C. P. M., Mamajek, E. E., & Naylor, T. 2015, MNRAS, 454, 593, doi: 10.1093/mnras/stv1981

Chang, S. W., Byun, Y. I., & Hartman, J. D. 2015, ApJ, 814, 35, doi: 10.1088/0004-637X/814/1/35

Chen, H., Zhan, Z., Youngblood, A., et al. 2021, Nature Astronomy, 5, 298, doi: 10.1038/s41550-020-01264-1

Christiansen, J. L., Jenkins, J. M., Caldwell, D. A., et al. 2012, PASP, 124, 1279, doi: 10.1086/668847

Curtis, J. L., Agüeros, M. A., Mamajek, E. E., Wright, J. T., & Cummings, J. D. 2019, AJ, 158, 77, doi: 10.3847/1538-3881/ab2899

Davenport, J. R. A., Covey, K. R., Clarke, R. W., et al. 2019, ApJ, 871, 241, doi: 10.3847/1538-4357/aafb76

Davenport, J. R. A., Hawley, S. L., Hebb, L., et al. 2014, ApJ, 797, 122, doi: 10.1088/0004-637X/797/2/122

Feinstein, A. D., Montet, B. T., Ansdell, M., et al. 2020, AJ, 160, 219, doi: 10.3847/1538-3881/abac0a

Feinstein, A. D., Seligman, D. Z., Günther, M. N., & Adams, F. C. 2022, ApJL, 925, L9, doi: 10.3847/2041-8213/ac4b5e

Feinstein, A. D., Montet, B. T., Foreman-Mackey, D., et al. 2019, PASP, 131, 094502, doi: 10.1088/1538-3873/ab291c

Foreman-Mackey, D., Hogg, D. W., Lang, D., & Goodman, J. 2013, PASP, 125, 306, doi: 10.1086/670067

Gagné, J., Fontaine, G., Simon, A., & Faherty, J. K. 2018, ApJL, 861, L13, doi: 10.3847/2041-8213/aacdff

Galindo-Guil, F. J., Barrado, D., Bouy, H., et al. 2022, A&A, 664, A70, doi: 10.1051/0004-6361/202141114

Gershberg, R. E. 1972, Ap&SS, 19, 75, doi: 10.1007/BF00643168

Goodman, J., & Weare, J. 2010, Communications in Applied Mathematics and Computational Science, 5, 65, doi: 10.2140/camcos.2010.5.65

Günther, M. N., Zhan, Z., Seager, S., et al. 2020, AJ, 159, 60, doi: 10.3847/1538-3881/ab5d3a

Hawley, S. L., Davenport, J. R. A., Kowalski, A. F., et al. 2014, ApJ, 797, 121, doi: 10.1088/0004-637X/797/2/121

Howard, W. S., & MacGregor, M. A. 2022, ApJ, 926, 204, doi: 10.3847/1538-4357/ac426e

Howell, S. B., Sobeck, C., Haas, M., et al. 2014, PASP, 126, 398, doi: 10.1086/676406

Ilin, E., Schmidt, S. J., Davenport, J. R. A., & Strassmeier, K. G. 2019, A&A, 622, A133, doi: 10.1051/0004-6361/201834400

Ilin, E., Schmidt, S. J., Poppenhäger, K., et al. 2021, A&A, 645, A42, doi: 10.1051/0004-6361/202039198

Kerr, R. M. P., Rizzuto, A. C., Kraus, A. L., & Offner, S. S. R. 2021, ApJ, 917, 23, doi: 10.3847/1538-4357/ac0251

Kounkel, M., Covey, K., & Stassun, K. G. 2020, AJ, 160, 279, doi: 10.3847/1538-3881/abc0e6

Luger, R., Bedell, M., Foreman-Mackey, D., et al. 2021, arXiv e-prints, arXiv:2110.06271. https://arxiv.org/abs/2110.06271

Luhman, K. L. 2007, ApJS, 173, 104, doi: 10.1086/520114

Maehara, H., Shibayama, T., Notsu, Y., et al. 2015, Earth, Planets and Space, 67, 59, doi: 10.1186/s40623-015-0217-z

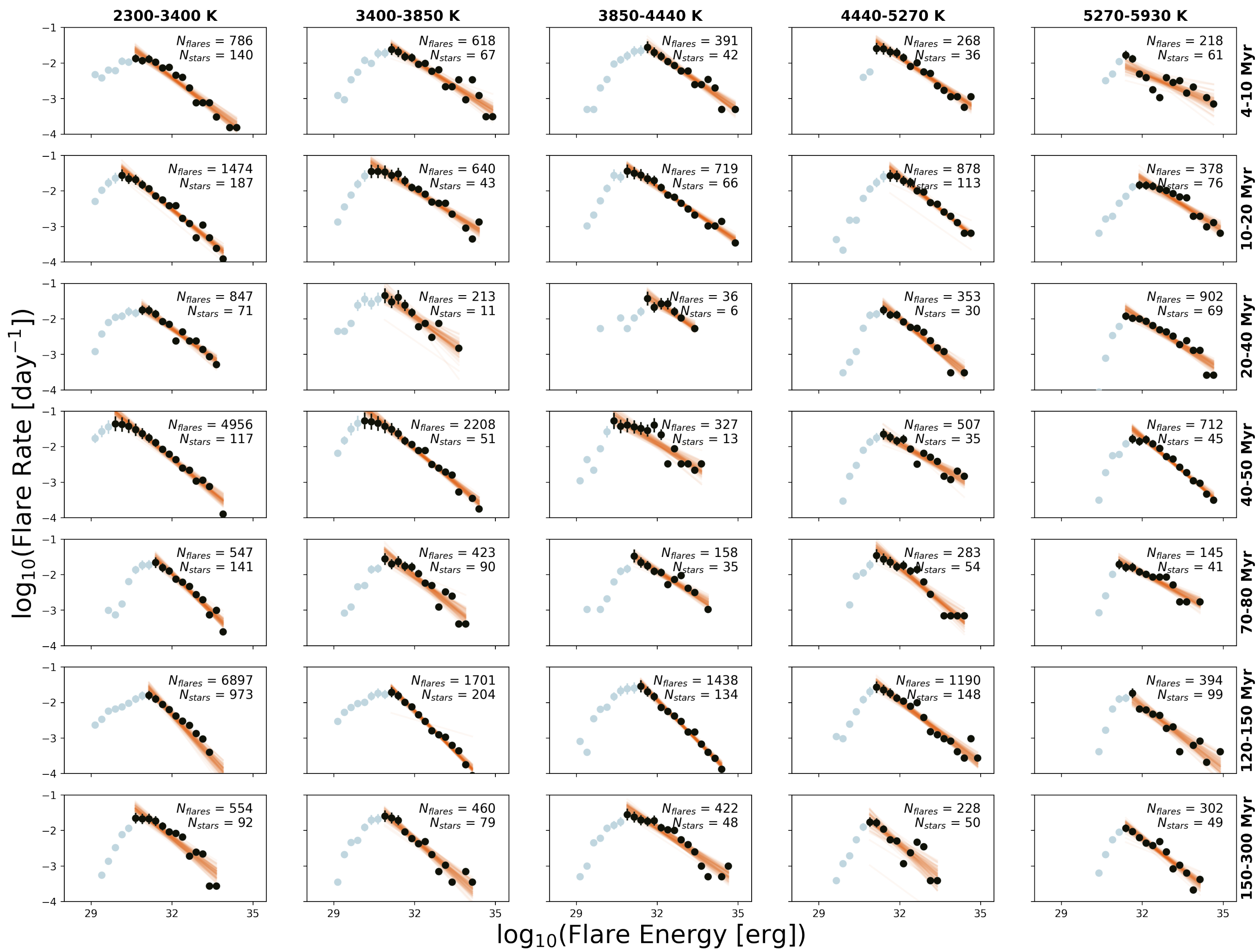

Figure A1. Flare frequency distributions (FFDs) for subgroups of stars, clustered by age and effective temperature, $T_{\rm eff}$. Flares were binned into 25 bins in log-space from $10^{27} - 10^{35}$ erg. We fit the FFD from the turn-over in the binned flares, likely a result of very low-energy flares being missed in our flare-detection algorithm. The bins used to fit the FFD are shown in black, while all bins are shown in gray. We ran an MCMC fit to these distributions with a simple power law; 100 random samples from these fits are over-plotted in orange. We fit distributions with > 3 bins. The best-fit slopes from these fits are presented in Figure 3.

Martin, D. C., Fanson, J., Schiminovich, D., et al. 2005, ApJL, 619, L1, doi: 10.1086/426387

Medina, A. A., Winters, J. G., Irwin, J. M., & Charbonneau, D. 2020, ApJ, 905, 107, doi: 10.3847/1538-4357/abc686

Morrissey, P., Conrow, T., Barlow, T. A., et al. 2007, ApJS, 173, 682, doi: 10.1086/520512

Murphy, S. J., & Lawson, W. A. 2015, MNRAS, 447, 1267, doi: 10.1093/mnras/stu2450

Notsu, Y., Shibayama, T., Maehara, H., et al. 2013, ApJ, 771, 127, doi: 10.1088/0004-637X/771/2/127

Okamoto, S., Notsu, Y., Maehara, H., et al. 2021, ApJ, 906, 72, doi: 10.3847/1538-4357/abc8f5

Pecaut, M. J., & Mamajek, E. E. 2016, MNRAS, 461, 794, doi: 10.1093/mnras/stw1300

Pizzolato, N., Maggio, A., Micela, G., Sciortino, S., & Ventura, P. 2003, A&A, 397, 147, doi: 10.1051/0004-6361:20021560

Ricker, G. R., Winn, J. N., Vanderspek, R., et al. 2015, Journal of Astronomical Telescopes, Instruments, and Systems, 1, 014003, doi: 10.1117/1.JATIS.1.1.014003

Röser, S., Schilbach, E., & Goldman, B. 2016, A&A, 595, A22, doi: 10.1051/0004-6361/201629158

Schneider, A. C., & Shkolnik, E. L. 2018, AJ, 155, 122, doi: 10.3847/1538-3881/aaaa24

Seligman, D. Z., Rogers, L. A., Feinstein, A. D., et al. 2022, ApJ, 929, 54, doi: 10.3847/1538-4357/ac5b69

Shibayama, T., Maehara, H., Notsu, S., et al. 2013, ApJS, 209, 5, doi: 10.1088/0067-0049/209/1/5

Silverberg, S. M., Kowalski, A. F., Davenport, J. R. A., et al. 2016, ApJ, 829, 129, doi: 10.3847/0004-637X/829/2/129

Tarricq, Y., Soubiran, C., Casamiquela, L., et al. 2021, A&A, 647, A19, doi: 10.1051/0004-6361/202039388

Tofflemire, B. M., Rizzuto, A. C., Newton, E. R., et al. 2021, AJ, 161, 171, doi: 10.3847/1538-3881/abdf53

Tovar Mendoza, G., Davenport, J. R. A., Agol, E., Jackman, J. A. G., & Hawley, S. L. 2022, AJ, 164, 17, doi: 10.3847/1538-3881/ac6fe6

Wright, N. J., Drake, J. J., Mamajek, E. E., & Henry, G. W. 2011, ApJ, 743, 48, doi: 10.1088/0004-637X/743/1/48

Wright, N. J., Newton, E. R., Williams, P. K. G., Drake, J. J., & Yadav, R. K. 2018, MNRAS, 479, 2351, doi: 10.1093/mnras/sty1670